Dual Orientation 16 MHz Single Element Ultrasound Needle Transducers for Image-Guided Neurosurgical Intervention

Yun Jiang, Zhen Qiu, Rachael McPhillips, Carl Meggs, Syed Osama Mahboob, Han Wang, Robyn Duncan, Daniel Rodriguez Sanmartin, Ye Zhang, Giuseppe Schiavone, Roos Eisma, Marc P.Y. Desmulliez, Sam Eljamel, Sandy Cochran, Tim W. Button, Christine E.M. Demore

Abstract—**Image-guided surgery is today considered to be of significant importance in neurosurgical applications. However, one of its major shortcomings is its reliance on preoperative image data, which does not account for the brain deformations and displacements that occur during surgery. In this work, we propose to tackle this issue through the incorporation of an ultrasound device within the type of biopsy needles commonly used as an interventional tool to provide immediate feedback to neurosurgeons during surgical procedures. To identify the most appropriate path to access a targeted tissue site, single-element transducers that look either forwards or sideways have been designed and fabricated. Micro-moulded 1-3 piezocomposites were adopted as the active materials for feasibility tests and epoxy lenses have been applied to focus the ultrasound beam. Electrical impedance analysis, pulse-echo testing and wire phantom scanning have been carried out, demonstrating the functionality of the needle transducers at ~16 MHz. The capabilities of these transducers for intraoperative image guidance were demonstrated by imaging within soft-embalmed cadaveric human brain and fresh porcine brain.**

Keywords—1-3 composite; needle ultrasound transducer; neurosurgery

I. INTRODUCTION

IMAGE guidance is routinely used in neurosurgery for intervention-related procedures including surgical planning, intra-operative navigation and lesion generation. Image-guided surgery usually relies on computed tomography (CT) scanning and magnetic resonance imaging (MRI) that are performed pre-operatively and not necessarily on the same day as surgery [1, 2]. The preoperative images however, may be inaccurate and unreliable as, once the skull is opened and the dura protecting the brain tissue is incised, brain shift and deformation can occur in response to various phenomena including raised intracranial pressure, cerebrospinal fluid leak, head-position alteration and tissue removal [3]. Maximum brain shifts of more than 20 mm have been reported [4, 5]. If not corrected, such significant inaccuracies between a predicted target location and its actual position could lead to a failure of target access, resulting, for example, in a false biopsy reading, and cause damage to normal tissue.

Different strategies have been reported to measure and correct brain shifts. Various biomechanical models have been developed for such estimation but so far no reliable prediction is possible [6, 7]. An objective, dynamic evaluation of the spatial position of brain tissue during surgery can only be provided by intraoperative imaging. Both intraoperative CT and MRI have demonstrated their usefulness in neurosurgical applications [8, 9], but these systems suffer from intrinsic disadvantages including interruption of the workflow during the intervention, difficult positioning of the patient, limited access for the surgeon to the operative field, and high cost.

In comparison, intraoperative ultrasound (IoUS) has recently attracted increasing interest not only because of its widely acknowledged safety, portability and low cost but also, and more importantly, its real-time visualisation capability. However, since existing neurosurgical IoUS systems require the ultrasound probe to be placed outside of the brain for guidance. Furthermore, multiple probes have to be used to suit different imaging targets in the brain [10-12], with frequencies of 7.5 - 10 MHz usually employed for the imaging of shallow or small regions and 3 - 5 MHz for deep-seated lesions [12]. The imaging resolution with these external probes is compromised to obtain the required imaging depth; higher frequency probes, with better image resolution, would result in too shallow an image to be useful for guiding surgery.

In order to overcome the drawbacks of current IoUS systems, we propose the integration of a single-element transducer at the tip of a biopsy needle, enabling neurosurgeons to visualise tissue through a burr hole in the skull at very close proximity with high-frequency, high-resolution transducers.

Since the idea of ultrasound in a catheter was first introduced in 1968 [13], a number of approaches for integrating ultrasound transducers and interventional tools have been proposed [14-19]. The majority of the reported miniaturised devices have been designed to be used as ultrasound biomicroscopes (UBM),

commonly for medical applications in ophthalmology and intravascular ultrasound imaging (IVUS), with housing diameters in the range 0.7 - 2.8 mm and the central frequency in the range 40 - 60 MHz [16-19]. Most of the prototypes are flat single element transducers in clinical practices such as IVUS, rather than miniaturised arrays. Although array transducers could provide more information, they are much more complicated and expensive, and suffer from various performance issues due to their small element size and weak signal to noise ratio. In terms of material selection, relaxor-based single crystals such as lead magnesium niobate - lead titanate (PMN-PT) and lead zinc niobate - lead titanate (PZN-PT) have become popular as electromechanically active materials because their exceptional piezoelectric properties offer improvements in sensitivity [17-19]. However, it is much more expensive and difficult to synthesise and machine those single crystals compared to PZT-based piezoceramics, and challenges still remain to fabricate high frequency (>30 MHz) single crystal composites. The choice of commercial silver-loaded epoxy as the backing material in the prototypes that have been reported is also open to improvement. Its conductive nature facilitates electrical connection from the rear of the active element; however, its acoustic impedance (~5 - 6 MRayl) is not well matched with that of single crystals, which may affect the overall performance of the transducer. In comparison, using non-conductive tungsten-loaded epoxy allows the acoustic impedance to be tailored to suit the damping needs of the transducer by varying the amount of tungsten [20].

In this work, two single element transducers were proposed to be integrated with needles of 1.8 mm inner diameter offering real-time forward and side viewing, respectively, to allow the neurosurgeon to manoeuvre safely on the way to the target site of interest. The inner diameter corresponds with that of commercially available biopsy needles frequently used in neurosurgical procedures. 1-3 piezocomposites were used as the active material because of their higher electromechanical coupling and lower acoustic impedance than single crystals and PZT-based piezoceramics [21, 22]. Tungsten-loaded epoxy (10 vol% tungsten) with acoustic properties matched with the 1-3 piezocomposites [20] was chosen as the backing material. The operating centre frequency for the transducers was designed to be 15 MHz, as this was considered to be sufficient to demonstrate the advantages of the needle-based device and it matches the operating frequency of commercially-available array instrumentation which will probably be used for future generations of transducer arrays integrated within needles. A range of tests was used to characterise the basic functionality of the ultrasound devices and the clinical feasibility of using needle transducers to guide and correct the path for intraoperative neurosurgical procedures was investigated using soft-embalmed cadaveric human brain [23] and fresh porcine brain.

II. FABRICATION METHODS

A. 1-3 Piezocomposites

Fabrication of piezocomposites was based on viscous polymer processing (VPP) which involves five main stages: (1) production of a piezoceramic paste; (2) embossing of pillar structures; (3) mould removal, drying and sintering; (4) filling the resulting bristle block with the polymer phase; and (5) lapping of the piezocomposites to thickness. A commercial PZT-5H type powder (TRS610C, TRS Ceramics, USA) with a primary particle size of 1.2 µm was used as the starting material.

Detailed process information has been reported previously in [24, 25] and Fig. 1(a) shows an optical micrograph of a VPP composite, in which cylindrical pillars with a diameter of ~20 µm and a kerf of ~8 µm are arranged hexagonally.
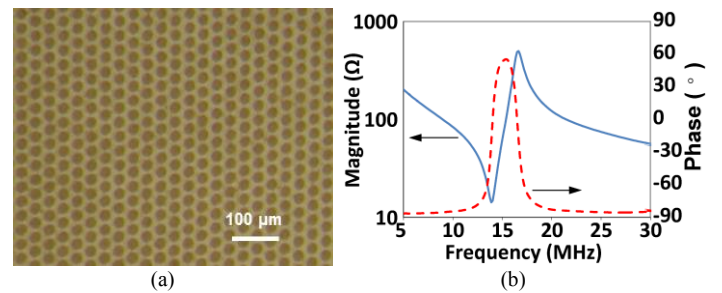

Fig. 1. (a) Top-view optical image of a typical VPP composite, where the darker areas are the pillars and the lighter area is the polymer matrix; (b) Impedance and phase diagrams of a 115 µm thick VPP composite.

The composites were carefully lapped to a thickness of ~115 µm using a PM5 lapping machine (Logitech, Glasgow, UK), giving resonant and anti-resonant frequencies around 14 MHz and 17 MHz respectively, as shown in Fig. 1(b), and effective coupling factors $k_{eff} \approx 0.6$. Poling of the composites was carried out in a bespoke corona poling jig at 120°C for 10 min with a voltage of 30 kV before depositing chrome-gold electrodes using a Peltier-cooled sputter coater (Emitech K575, Emitech Ltd., UK). The composites were then laser-cut into discs with a diameter of 1.7 mm, ready for transducer fabrication. The transducers incorporating the composites facing forwards and sideways are named FF and SF, respectively.

B. Single element needle transducers

Considering the possible use of MRI in conjunction with ultrasound imaging for neurosurgical procedures, MRI compatibility of the device is essential. Non-magnetic brass tubes (Speciality Metals, UK) were used as casings, with length, inner diameter (ID) and outer diameter (OD) of 80 mm, 1.8 mm and 2.4 mm, respectively. The casing used for SF had a longitudinal opening of 3 mm near the tip.

The detailed fabrication processes for both the forward-facing and side-facing needle transducers are shown schematically in Fig. 2 and a summary of the dimensions and key properties of the transducers is given in Table 1. The longitudinal sound velocity (V_l) of the composite material was

calculated from its measured anti-resonant frequency and sample thickness, V_l of the backing material was measured from previous work [20] and V_l of the lens was measured in this work using through transmission characterisation technique [26].

For the forward-facing transducer, an enamelled copper wire with a diameter of 80 µm was connected to the back electrode of the active material with silver epoxy (RS Components, UK) to act as the signal connection. A cast-in-place process was then used for the tungsten-loaded epoxy backing. After curing at room temperature, the whole assembly was inserted into the case and a micro-coaxial (MCX) connector was soldered onto the wire and then glued into the end of the needle. After the gap between the transducer and the needle had been carefully filled with Epofix epoxy (Struers, UK), a gold film was sputtered on to the front surface of the transducer within the needle to make the ground connection.

For the side-facing transducer, a tungsten-loaded epoxy insert was fabricated to fit the lateral opening of the needle. A hole of ~300 µm diameter was drilled through the insert to provide access for the signal wire to be connected to the bottom electrode. The piezocomposite was then mounted on the insert before fitting the completed assembly into the needle. A small amount of tungsten-loaded epoxy around the edge of the active material provided electrical insulation prior to sputtering gold over the whole area of the insert to make the ground connection.

Fig. 3 shows a pair of assembled needle transducers, one orientated forwards and one sideways, together with close-up images of composites mounted in the needles. In the close-up pictures of FF and SF some of the extra epoxy or tungsten-loaded epoxy, which has been added to the edges of the composites to avoid electrical shorting, has impinged on the exposed surfaces, resulting in slight deviations from the intended circular shapes though with negligible influence on the properties of the transducers.
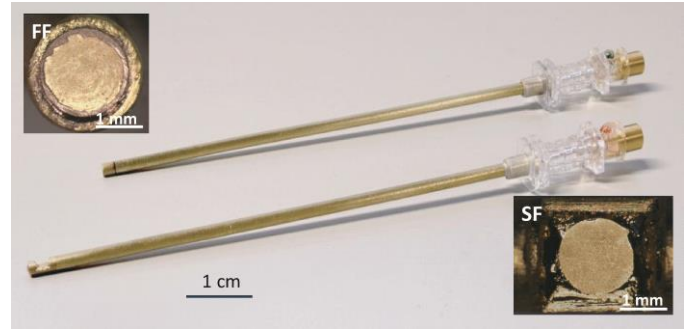

Fig. 3.   Photographs of single-element transducers in needles. The two inset images show the foward-facing (FF) and side-facing (SF) transducers.
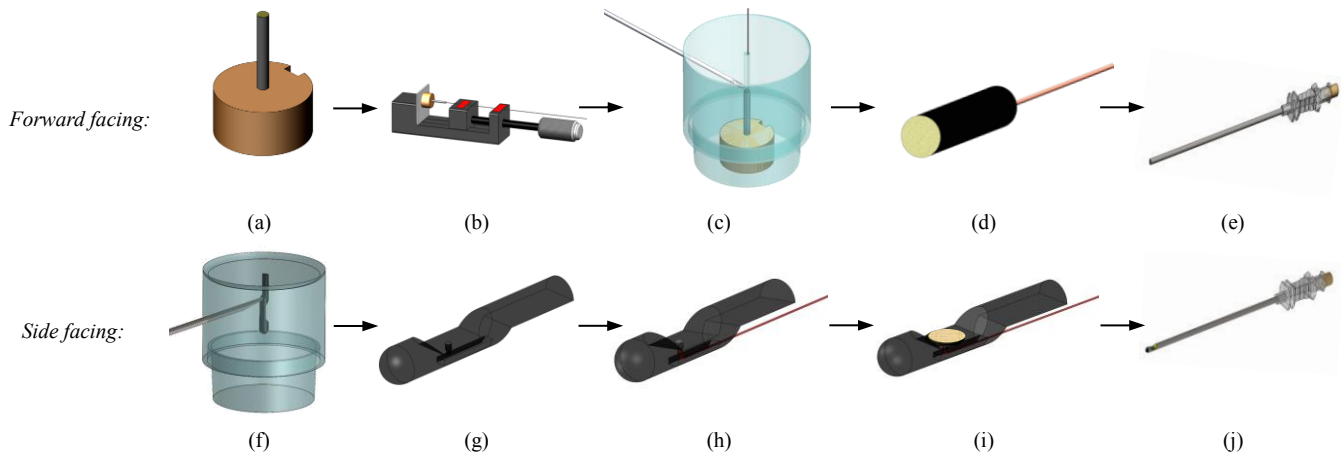

Fig. 2.   Fabrication processes for both (a) - (e) forward-facing, and (f) - (j) side-facing needle transducers. For the forward-facing transducer: (a) A piezocomposite disc was mounted with wax on a 1.8 mm diameter drill shaft fixed in a brass base; (b) the brass former with the piezocomposite disc was stuck to one side of a mini vice. A single core wire with the end dipped in silver-loaded epoxy was taped down to the other end. Electrical connection was achieved by closing the vice jaws to bring the composite face towards the end of the wire; (c) after curing, the brass former with piezocomposite disc and wire was slid into a soft mould for the cast-in-place tungsten-loaded epoxy backing; (d) tungsten-loaded epoxy was then cured at room temperature before the whole assembly was inserted into a housing. (e) After soldering an MCX connector to the wire, the front face of the needle was sputtered with gold for the ground connection. For the fabrication of the side-facing transducer: (f) moulding of a tungsten-loaded epoxy backing insert was performed with a soft mould which was cast from a brass former machined to the required shape; (g) after curing, the backing insert was demoulded and an access hole with a diameter of ~300 µm was drilled into the backing to accommodate a wire; (h) a wire was fed through the hole and fixed to the insert with silver epoxy; (i) a piezocomposite disc was attached to the insert with a small amount of silver-loaded epoxy; (j) the whole assembly was inserted into a needle. A small amount of tungsten-loaded epoxy was added around the edge of the piezocomposite disc to prevent it from shorting before gold-sputtering the front face of the piezocomposite disc and the needle to create a ground connection.

TABLE 1 SUMMARY OF THE COMPONENTS OF NEEDLE TRANSDUCERS.

Component	Material	Dimensions (mm)	Longitudinal sound velocity (m/s)	Acoustic Impedance (MRayl)
Needle housing	Brass	$\Phi(ID=)$1.8 , $\Phi(OD)$=2.4, $length$= 80	N/A	N/A
Active element	1-3 PZT-based composites	Φ=1.7, $thickness$ (th)=0.115	3674	14
Backing	Tungsten epoxy	FF: th = 5 SF: semi-cylindrical, r = 0.9	1712	5
Concave Lens	Specifix-20 epoxy	Φ=1.8, Radius of curvature: 4.37, th at center: 0.044, th at edge: 0.127	2883	3

C. Lens

Concave epoxy lenses (Specifix-20, Struers Ltd., UK) were included in the design to focus the ultrasound beams. The diameter and the radius of curvature of the lens were 1.8 mm and 4.37 mm, respectively. The thickness of the lens at the centre was designed to be a quarter of the wavelength in epoxy, 43.8 µm, to minimise internal reflection and the thickness of the lens at the edge was 127 µm.

The acoustic field of the needle transducer with the lens attached was simulated using the finite element modelling software, PZFlex (Weidlinger Associates Inc., Mountain View, CA, USA). Fig. 4(a) shows the 2D model built for FF, with the physical and functional parameters of each component listed in Table 1. Absorbing boundary conditions were applied at all edges of the model. The driving signal to the transducer was a single cycle, 1 Volt (peak to peak voltage) sinusoidal wave, and the acoustic pressure output of the transducer was normalized by the electrical input on the composite. The simulated ultrasound beam pattern is presented in Fig. 5, with resolution of 4.5 nm in both lateral and axial directions. An obvious focusing zone can be seen, and the maximum pressure point, i.e. focal point, appears 5.81 mm in front of the transducer. The -6 dB contour of focal area is 7.47 mm in the axial direction, and 0.42 mm in lateral direction.

The lenses were moulded using a steel ball bearing with the desired curvature and a metal ring cut from a brass needle housing and lapped to the required edge thickness of the lens. After being checked for defects with an optical microscope, the fabricated lenses were mounted on the transducer faces using a small amount of epoxy. Fig. 4(b) shows an optical image of an epoxy lens with an acceptably small number of air bubbles for a prototype device.
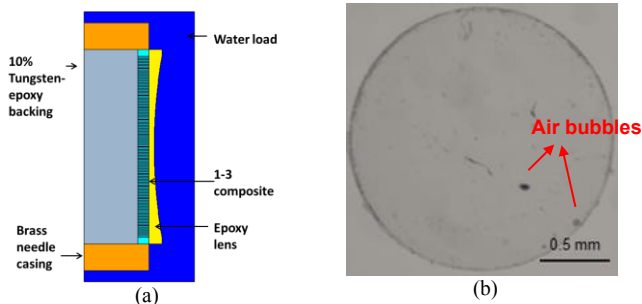

Fig. 4. (a) Schematic drawing of FF with lens attached; (b) optical image of an epoxy lens fabricated with a diameter of 1.8 mm.
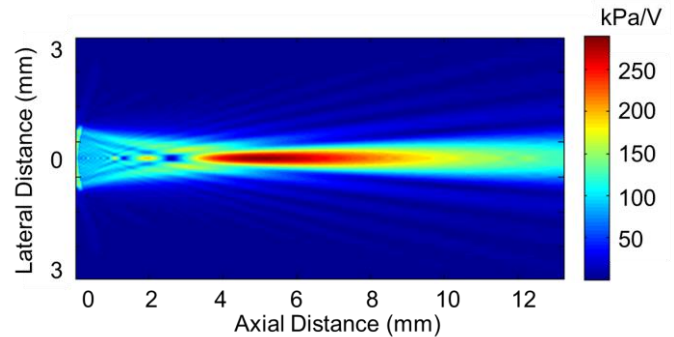

Fig. 5. Ultrasound beam pattern simulated using a finite element model of the foward-facing needle transducer.

III. TRANSDUCER CHARACTERISATION

A. Impedance analysis

The electrical impedance spectra of the two assembled needle transducers, with lenses attached, were measured in water with a precision impedance analyser (4395A, Agilent Technologies UK Ltd., UK), and the results are presented in Fig. 6. The damping introduced by the backing layer and the lens in each case has significantly reduced the variation in impedance magnitude and phase around the resonances, in comparison to that of the composite shown in Fig. 1(b). It is therefore difficult to identify the precise resonance frequencies from the figures, especially for FF which has a thicker backing layer attached. However, it is clear that the resonances of both transducers are in the range 15 – 20 MHz. The smaller features away from the main resonance peaks in the result for SF were not observed while characterising the piezocomposite discs prior to assembly. They are related to the physical limitation of the thickness of the backing to less than 1 mm in this device because of the small needle diameter; in contrast, the backing in the forward-facing device was around 5 mm thick, resulting in a cleaner, and more damped, impedance curve.
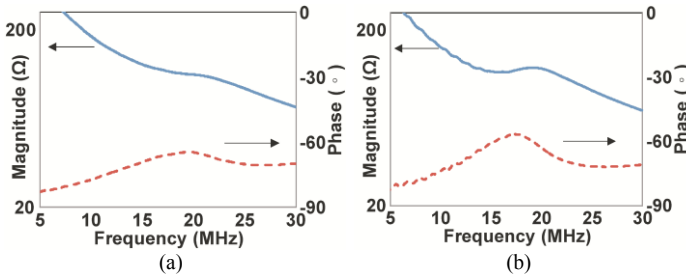
Fig. 6. Electrical impedance magnitude and phase diagrams of (a) FF and (b) SF measured in water.

B. Pulse-echo tests

The pulse-echo responses of the transducers were measured using a high frequency pulser-receiver (DPR 500, JSR Ultrasonics, Pittsford, NY, USA). The pulser energy was selected to be 12.4 µJ, and pulse repetition frequency (PRF) was 1 kHz. No gain was applied to the received signal. The transducers were positioned in a degassed water bath and a flat, aluminium block submerged in water was placed at the actual focal point, as measured by the maximal reflected signal, to act as a target. The results were recorded using an oscilloscope (MDO3024, Tektronix, Oregon, USA) and are shown in Fig. 7. After applying a fast Fourier transform (FFT) to the signal, the centre frequency and -6 dB percentage bandwidth were calculated, and listed in Table 2. The amplitude of the echo signal was recorded to determine relative sensitivity. The pulse length was recorded as the length of time between the first and last points -20 dB down from the peak amplitude. SF showed a narrower bandwidth and corresponding longer pulse than FF.
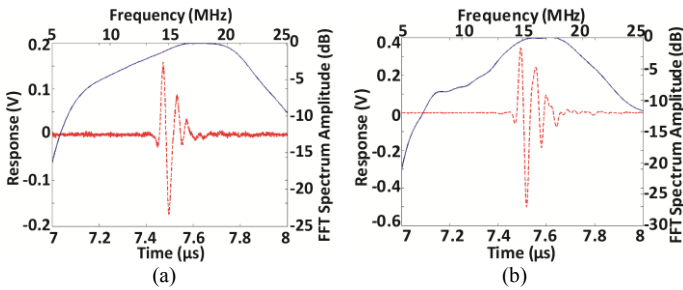

Fig. 7. Pulse-echo response and spectrum of (a) FF and (b) SF.

TABLE 2 PARAMETERS OF NEEDLE TRANSDUCERS FROM PULSE-ECHO TESTS.

	FF	SF
Centre frequency (MHz)	16.97	16.14
BW %	88.6%	60.4%
Pulse Length (µs)	0.08	0.10
Sensitivity (mV)	340	830
Insertion loss (dB) at 16 MHz (after compensation)	38.4	30.5

The two way insertion loss of each device was measured following a method described elsewhere [27]. The measured values were then compensated for loss because of attenuation in the water bath (2×10^{-4} dB/mm-MHz^2) [28], and reflection from the aluminium target (reflection coefficient from water to aluminium: 0.862). The insertion loss values are higher than the figures of 15 - 25 dB reported for piezocrystal needle transducers [18, 29, 30] but are still comparable with those of some 1-3 PZT composite transducers [31, 32]. FF suffers about 8 dB more loss than SF, consistent with the indication of higher damping illustrated in Fig. 6, where the variation around the resonance is smaller. There are several possible reasons for this, related to the individual fabrication processes of both the piezocomposites and the ancillary components. However, even with this higher insertion loss, FF has sufficient performance for the feasibility studies carried out in this work.

C. Wire phantom scan

The imaging capabilities of the needle transducers were studied by scanning wire phantoms. The transducers were connected to a scanning system built in-house, with software programmed with LabVIEW (National Instruments, Newbury, UK). Both FF and SF were attached to an automatic linear scanning stage with a SHOT-602 controller (Sigma Koki, Tokyo, Japan), and the reflected echoes were captured and saved with an oscilloscope, later being imported into MATLAB (The MathWorks Inc., Cambridge, UK) for image analysis. Two wire phantoms were prepared. For FF, the phantom had eight tungsten wires 20 µm in diameter, positioned in a bespoke holder so that they were separated by ~1 mm along the axial and lateral directions. For SF, a radial wire phantom was made with a holder produced by rapid prototyping in which several nylon fishing wires of 0.7 mm diameter were positioned at various radial distances.

Linear scans were performed with FF moving in lateral steps of 0.02 mm over the tungsten wire phantom. The transducer was carefully positioned such that the first wire was 2.8 mm from the transducer and the fourth wire about 5.8 mm, at the predicted focal distance. For SF, the system configuration was similar but the transducer remained in a fixed central position with the radial phantom mounted on a motorized precision rotation stage (PRM1Z8 mount with TDC001 T-Cube DC Servo Motor Controller, Thorlab, New Jersey, USA) and rotated around 120° in 0.2 degree steps. All scans were carried out with both the transducers and phantoms submerged in water and the images are displayed with a dynamic range of 35 dB.

Fig. 8 shows the linear and rotational images obtained with FF and SF, respectively. Both images have relatively good resolution, especially in the axial direction. The linear scanning image was used to evaluate the beam width and resolution of FF. Fig. 9 shows the point spread function near the focal point, extracted from Fig. 8(a). For this particular plot, the maximum pressure is detected at time corresponding to 5.85 mm from the transducer. Its dimensions at the -6 dB contour are 0.47 mm laterally and 0.062 mm axially, corresponding to the lateral and axial resolutions of FF, respectively. To understand more about the beam pattern, similar plots were produced for the other seven reflecting targets, and the lateral dimensions -6 dB down from the peak amplitudes are shown in Fig. 10, along with the corresponding data extracted from the simulated field presented in Fig. 5 for comparison. It can be seen that there is good agreement between the experimental and simulated results.
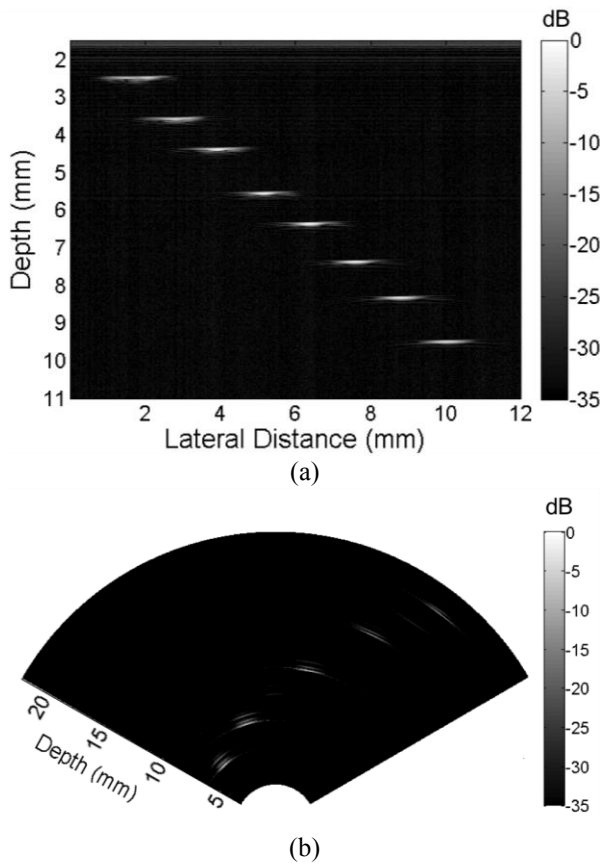
(a)

(b)

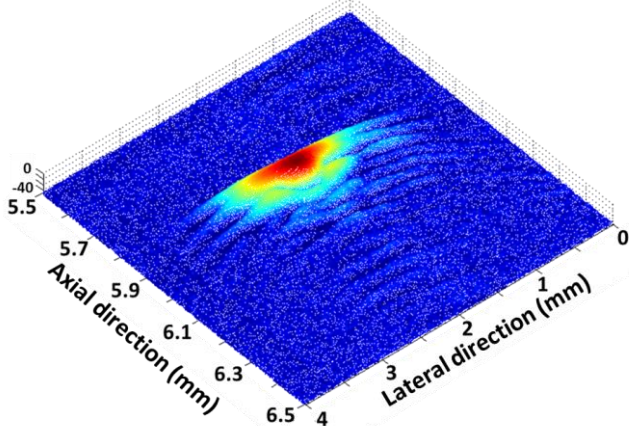Fig. 8.   B-scan images of phantoms from (a) FF and (b) SF.

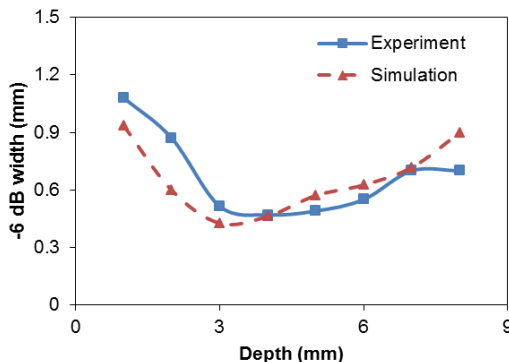Fig. 9.   Point spread function near the focal point of FF. Axial scale exagerated relative to lateral scale.

Fig. 10. Comparison of measured and simulated lateral resolutions for FF.

D.   M-mode imaging of soft-embalmed human cadaveric brain

After basic characterisation, feasibility tests exploring the viability of clinical procedures were done by a neurosurgeon (author SOM). The guidance potential of the needles was tested using the brain of a soft-embalmed human cadaver, donated to the Centre of Anatomy and Human Identification at the University of Dundee in accordance with the Human Tissue (Scotland) Act, 2006. A cadaver soft-embalmed with the Thiel process was selected for this work because of its availability and lifelike flexibility and tissue quality, compared to traditionally embalmed rigid cadavers [23, 33], which would have been unsuitable for the work reported here. The specific cadaver selected had no known medical conditions affecting the brain and it was four-week post-embalming when the experiment was conducted. The cadaver remained intact except for the burr hole in the skull noted below.

The experimental set-up was similar to what has been described previously for generating B-mode images, except that FF and SF were manually held by the neurosurgeon and inserted into the brain. The movement of the imaging needle was restricted to some extent by the entry path into the brain created during insertion. This in turn made the commonly adopted B-mode scans unsuitable and, instead, M-mode (motion mode) scans were used in this feasibility study to provide real-time guidance.

As illustrated in Fig. 11, for FF, the needle was manipulated along the access path such that the distance between the needle tip and the target was varied. Similarly, SF was inserted into the tissue and rotated until the target was identified. As the needles were manoeuvred within the tissue, A-scan data were captured continuously, with a recording rate of 6 A-scans per second, and displayed as an M-mode image to provide a real time visualisation of the distance between the target and the needle transducer.
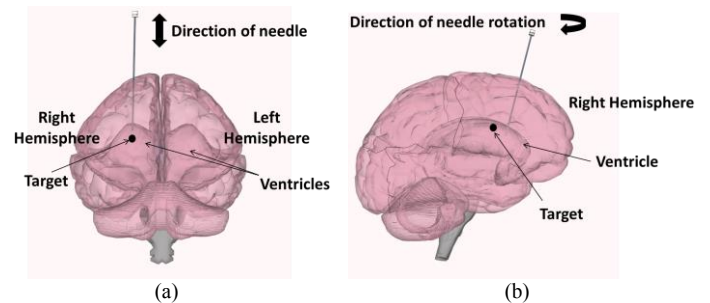

(a)

(b)

Fig. 11. Diagram of M-mode imaging experimental set up (a) target in front of FF (b) target at side of SF (after [34]).

An initial MRI scan of the cadaveric brain was performed to assess its general state including its gross volume, grey/white matter differentiation and state of the ventricles prior to the opening of the skull and penetration of the needle. As presented in Fig. 12(a), the MR image shows that the selected cadaver had good brain volume and well-preserved architecture, allowing for a clear differentiation between grey and white matter prior to intervention. This agrees with the characteristics of the MRI scans of soft-embalmed cadavers reported by Eljamel et al. [35] and Gueorguieva et al. [36]. After placing the cadaver in the supine position, a burr hole ~1 cm in diameter was created in the skull in the midpupillary line (above pupil) 2.5 cm from

midline and 1 cm in front of the coronal suture (Kocker's point) as the opening of the intraoperative path for the needle transducers.

Modelling clay (Play-Doh™) was chosen as the target material to provide an acoustically contrasting boundary within the brain. Fig. 13 shows the 8 - 10 mm diameter targets prepared for the experiment. The target was inserted through the burr hole and seated deeply in the brain. The needle was inserted into the tissue through the same burr hole as the target, but along a parallel track for each needle, and navigated into the brain tissue until a signal from the target was identified on the display. M-mode images were acquired with both FF and SF needles.
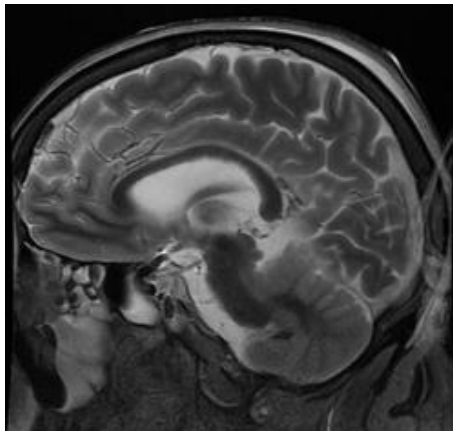
(a)
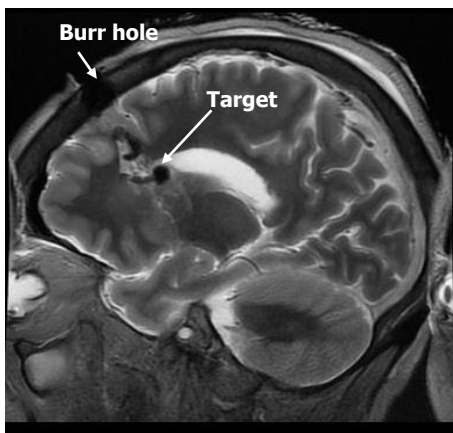
(b)

Fig. 12. T2-weighted MRI of cadaveric brain, sagittal view, (a) prior to experiment and (b) post intervention. Grey matter appears bright and white matter dark in the images
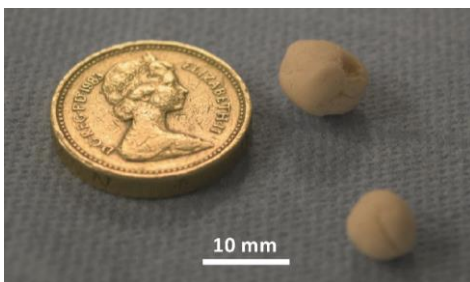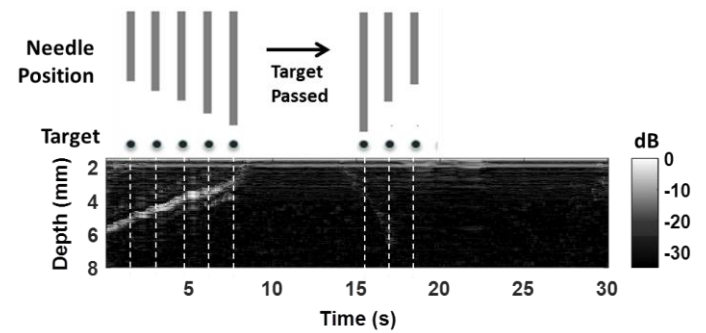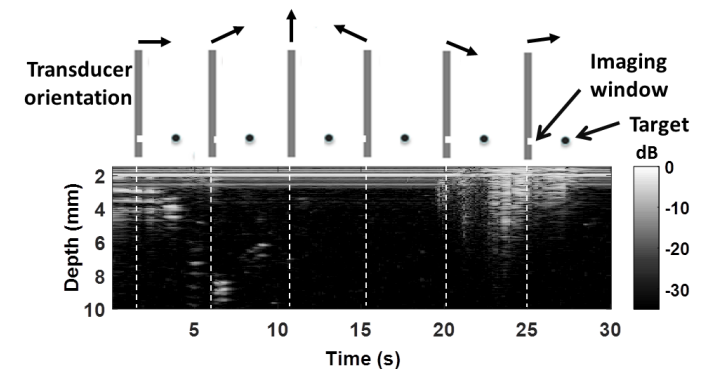

Fig. 13. Image of modelling clay targets.

Fig. 14(a) and (b) present the M-mode images generated while inserting FF and rotating SF, respectively. The images are displayed with 35 dB dynamic range. The bright dots in the figures indicate the target position. As the needle was inserted into the brain, the depth of the target shown in the M-mode image was reduced, indicating the needle tip was approaching the target. Similarly, as the needle was drawn back, the depth of the target was increased meaning the distance from the needle tip to the target was increased. This confirms the feasibility of using a forward-facing ultrasound needle transducer to guide and correct the path for intraoperative surgical procedures. When imaging with SF, the target can be detected initially before it disappears as the needle is rotated and as a result is no longer in the field of view of the transducer. The target then reappears as the needle is rotated 360º.

(a)

(b)

Fig. 14. M-mode imaging results of cadaveric brain tissue with modelling clay target aquired by (a) FF and (b) SF. The depths of the high brightness regions in the grey-scale images demonstrate the relative distances between the transducers and the target. Illustrative diagrams above the images demonstrate the relative positions of the needles and the target.

MRI scanning was repeated following the surgical experiment to assess the location of the target and to correlate this with the signals acquired by the needle, as shown in Fig. 12(b). The target can be seen in the ventricle, with the skull opening clearly visible. Substantial damage of the brain tissue structure can be observed by comparing Fig. 12(b) with Fig. 12(a). There are several factors that might have caused the damage. The brain quality may have deteriorated in the process placing the relatively large modelling clay target, or the repeated insertions of the needles during the experiment. In clinical use, the number of needle insertions permitted would be strictly minimised in order to keep the damage caused by the needle to a minimum. The deterioration of the tissue at the site

of the experiment can also be attributed to the delicate nature of the soft-embalmed brain [37]; Thiel embalmed brains are known to lose their structural integrity when handled. Although this limits the range of invasive procedures that can be performed, Thiel soft-embalmed cadavers remain a valuable research asset in neurosurgery considering their life-like quality and well-preserved brain anatomy.

### E. M-mode imaging of fresh porcine brain

A follow up experiment was performed with fresh porcine brain to further examine the performance of the ultrasound imaging needles with fresh brain tissue. Fresh brain tissue has the consistency closest to that of live animals. Therefore, this experimental procedure can be used as a feasibility study for *in vivo* procedures. All the imaging tests were performed within a few minutes of the death of the pig.

Following the same experimental procedure described in the previous section, an initial MRI scan was performed prior to the opening of the skull. The coronal view of the MRI scan is shown in Fig. 15(a). Two burr holes, instead of one, were then created in the Parietal region of the porcine skull so that insertions of the target and the needle could be made via different paths, as shown in Fig. 16. A modelling clay target about 10 mm in diameter was prepared and inserted carefully into the brain from burr hole-1 and left in place. The ultrasound imaging needle was inserted from the adjacent burr hole-2. Water-based ultrasound coupling gel (H361260G, Henleys Medical Supplies, Hertfordshire, UK) was dispensed into the burr hole-2 prior to needle insertion, to fill the possible air gaps between the needle and the brain tissue that may potentially affect the imaging quality.

The M-mode scans were generated with both FF and SF needles with 10 A-scans per second acquired over 20 s. The resulting images are displayed in Fig. 17, with a dynamic range of 35 dB. Similar to the M-mode imaging in the embalmed cadaver brain, the scan with FF (Fig. 17(a)) indicates the varying axial distance between the needle tip and the target, while the scan with SF Fig. 17(b)) indicates the lateral orientation of the target relative to the needle, with the target detected when in the field of view of the transducer.
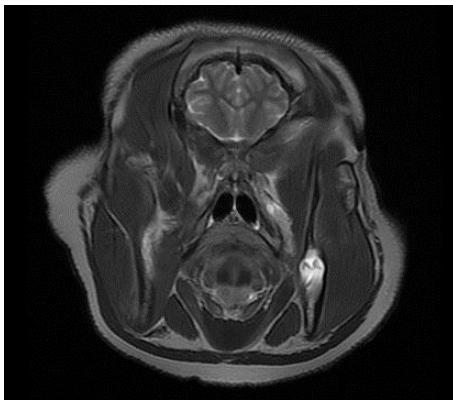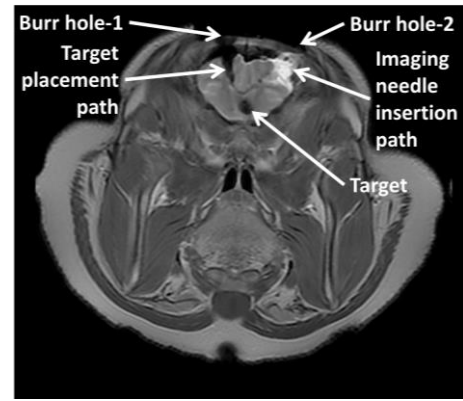
(b)

Fig. 15. T-2 weighted MRI of porcine brain in coronal view, (a) prior to the experiment and (b) post imaging needle intervention. The water-based ultrasound gel filled in burr hole-2 appears bright in the MRI under burr hole-2.
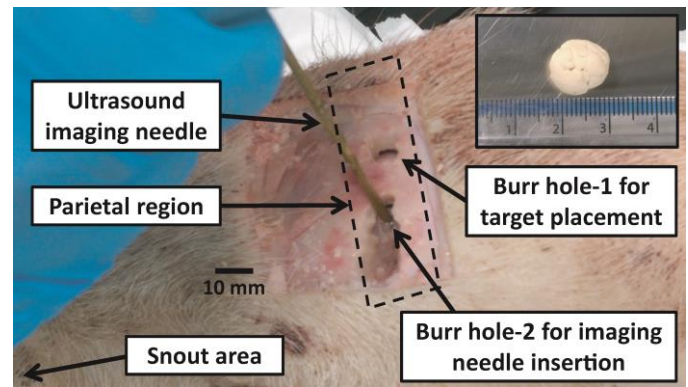
Fig. 16. Photograph demonstrating two burr holes opened on the porcine skull for target placement and imaging needle insertion, respectively. The inset photo shows the dimension of the modelling clay target.

Post-intervention MRI was performed and is presented in Fig. 15(b). Two burr holes are clearly visible on the porcine skull in the MR image. A noticeable insertion path appears in the brain tissue under burr hole-1, with the modelling clay target shown in the ventricle. However, the MR image indicates there is no significant damage to the brain tissue under burr hole-2 even after repeated needle insertions and imaging experiments.

(a)
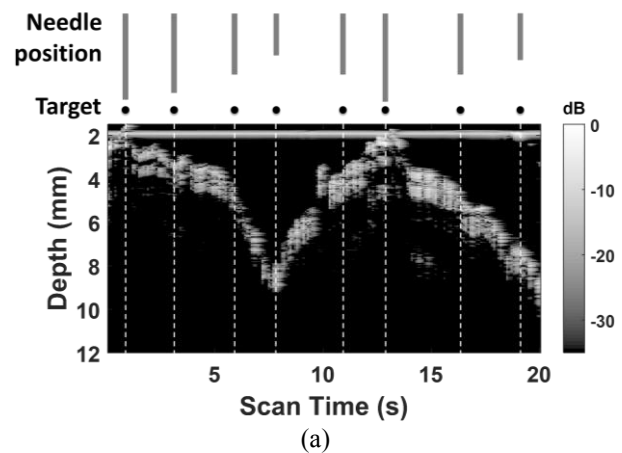
(a)

Fig. 17. M-mode imaging results of fresh porcine brain tissue with modelling clay target aquired by (a) FF and (b) SF. The depths of the high brightness regions in the grey-scale images indicate the relative distan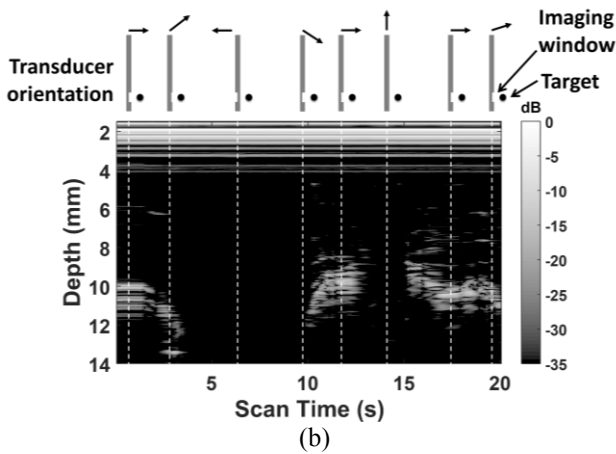ces between the transducers and the target. Illustrative diagrams above the images demonstrate the relative positions of the needles and the target.

IV. DISCUSSIONS

Differences in performance between the two transducers with the same constituent materials but different orientations were noted from the characterisation results. Firstly, SF has a narrower bandwidth than FF. This is attributed to the thin, semi-cylindrical backing layer of SF, imposed by the diameter of the needle. A possible solution is to introduce more damping by increasing the tungsten volume fraction in the backing material, with a resulting compromise in the sensitivity. This trade off can be optimised with further simulation. Secondly, FF suffers from higher insertion loss and hence lower sensitivity. This could be partially caused by the difference in the backing layer, but other contributory factors are likely to be involved, as the insertion loss values for both transducers are higher than expected. Some of the fabrication steps such as the electrical connection to the composite and the addition of the lens, as well as the characterisation conditions such as the length of the cables need optimised to help identify the causes and develop solutions.

Similar penetration depths of ~10-15 mm were found for both transducers during imaging. Although this is shallow for 16 MHz transducers, the imaging depth is limited by the focal depth of the transducers (about 6 mm), and the beam spread is too broad to image beyond about 12 mm, as illustrated in Fig. 5. The image penetration depth can be improved by increasing the focal depth of the lens, with corresponding increase in beam waist, and by improving the overall sensitivity of the transducers and system as discussed above.

In the study of brain tissue imaging, the ideal experimental configuration would be to insert a human tumour tissue into a cadaver brain. However, implementing such a procedure would require extensive preparation and optimisation for regulatory and ethical approval. As commonly observed in clinical practice, brain tumours can resemble materials ranging from stony (hard) to soft cheese in stiffness; modelling clay is a highly acceptable material to mimic tumours in this context. A further reason to use modelling clay is that it is compatible with MRI; it is also readily available and can be moulded to size and shape as required.

Real-time M-mode ultrasound images were acquired with single-element transducers on both FF and SF needles during needle insertion procedures in both the cadaveric brain tissue and fresh porcine brain tissue. It is useful to address here that after the few experiments with Thiel human brain and fresh porcine brain, the neurosurgeon who performed the intervention had gained sufficient experience and understanding of real-time M-mode images to be able to locate the target more effectively in later experiments.

The intervention in the porcine brain did not substantially damage the tissue as was observed in the embalmed cadaveric brain. It is therefore reasonable to suspect that in the initial experiments with the cadaveric brain, the structure of the tissue was likely damaged during target placement, prior to the needle insertions. The causes of this are both the insertion of the relatively large target and poor structural integrity the embalmed brain tissue when handled. The problem of tissue damage within the imaging region was avoided in the porcine specimen by using separate burr holes for target placement and needle insertion.

Based on the experience from this work, integration of two single-element transducers offering different orientations within a needle seems relatively straightforward. However, for optimal performance, several key design factors need to be taken into account, including the distance between the transducers, the dimensions and composition of the backing, the electrical connection method and the assembly sequence.

Although the concept of 'ultrasound in a needle' for image guided neurosurgery has been demonstrated in this work, the information obtained by the single-element transducers is still limited in comparison to array-based devices offering dynamic focusing and larger imaging depths. 16-element and 64-element 15 MHz linear arrays can be designed to fit in the same needle, looking forwards and sideways, respectively. However, array needle transducers suffer from a range of fabrication challenges including array patterning and device packaging in such a confined space, as well as various performance issues caused by small elements and long signal paths. Also, the operating procedures and the learning process for the neurosurgeons would be increasingly complicated and time-consuming. The successful tests of the single-element transducers reported here suggest that, just as with IVUS, they may balance price, viability, practicality and performance sufficiently for surgical adoption.

V. CONCLUSIONS

Two 16 MHz focused single element needle transducers designed for intraoperative image-guided neurosurgery have been constructed using micro-moulded 1-3 piezocomposites. Different techniques were developed for the fabrication of the transducers facing forwards and sideways. The -6 dB bandwidths of FF and SF are 88.6% and 60.4%, respectively, and the insertion losses are 38.4 dB and 30.5 dB. The M-mode images acquired from the two clinical feasibility studies indicate the significant potential of the ultrasound needle

devices to identify targets within brain tissue in a minimally invasive procedure.

The basic procedure outlined in the neuroimaging of both Thiel cadaveric human brain and fresh porcine brain can be likened to the practice of guiding a biopsy needle towards a tumour position. Forward-facing ultrasound transducers can be used to guide a biopsy needle safely into tissue, avoiding critical structures such as blood vessels in the brain. Once the needle is positioned accurately at the tissue region of interest, the sideways-viewing ultrasound transducer can offer accurate tissue diagnostics and targeting.

In future work, a needle incorporating dual-orientation single element transducers will be assembled. This may be followed by the development of a dual-orientation array needle with 16-element and 64-element linear arrays to look forwards and sideways, respectively. In the meantime, many features of needle transducers can be improved to further explore similar applications and the effective guidance of needles in neurosurgery, playing a crucial role in needle-based procedures such as EVD (external ventricular drain), VP (ventriculoperitoneal) shunt, lumbar drain, deep brain electrode insertion and biopsy of various lesions.

Acknowledgments

References

[1]   T. M. Peters, "Image-guided surgery: from X-rays to virtual reality," *Computer Methods in Biomechanics and Biomedical Engineering,* vol. 4, pp. 27-57, 2001.

[2]   A. G. Filler, "The history, development and impact of computed imaging in neurological diagnosis and neurosurgery: CT, MRI, and DTI," *Nature Precedings,* vol. 7, pp. 1-69, 2009.

[3]   D. L. Hill, C. R. Maurer Jr, R. J. Maciunas, J. A. Barwise, M. J. Fitzpatrick, and M. Y. Wang, "Measurement of intraoperative brain surface deformation under a craniotomy," *Neurosurgery,* vol. 43, pp. 514-526, 1998.

[4]   P. Hastreiter, C. Rezk-Salama, G. Soza, M. Bauer, G. Greiner, R. Fahlbusch, O. Ganslandt, and C. Nimsky, "Strategies for brain shift evaluation," *Medical image analysis,* vol. 8, pp. 447-464, 2004.

[5]   M. M. J. Letteboer, P. W. Willems, M. A. Viergever, and W. J. Niessen, "Brain shift estimation in image-guided neurosurgery using 3-D ultrasound," *Biomedical Engineering, IEEE Transactions on,* vol. 52, pp. 268-276, 2005.

[6]   M. P. Sindou, *Practical handbook of neurosurgery*: Springer, 2009.

[7]   C. Nimsky, O. Ganslandt, P. Hastreiter, and R. Fahlbusch, "Intraoperative compensation for brain shift," *Surgical Neurology,* vol. 56, pp. 357-364, 2001.

[8]   E. Alexander III, T. Moriarty, R. Kikinis, P. Black, and F. Jolesz, "The present and future role of intraoperative MRI in neurosurgical procedures," *Stereotactic and functional neurosurgery,* vol. 68, pp. 10-17, 1997.

[9]   S. Zausinger, C. Schichor, E. Uhl, M. F. Reiser, and J.-C. Tonn, "Intraoperative CT in Neurosurgery," in *Intraoperative Imaging and Image-Guided Therapy*: Springer, 2014, pp. 529-536.

[10]   L. M. Auer and V. Velthoven, *Intraoperative ultrasound imaging in neurosurgery*: Springer Science & Business Media, 1990.

[11]   H. Tang, H. Sun, L. Xie, Q. Tang, Y. Gong, Y. Mao, Q. Xie, M. Zheng, D. Wang, and H. Zhu, "Intraoperative ultrasound assistance in resection of intracranial meningiomas," *Chinese Journal of Cancer Research,* vol. 25, p. 339, 2013.

[12]   R. Sawaya, "Radical resection of glioblastoma: techniques and benefits," *Contemporary Neurosurgery,* vol. 24, pp. 1-5, 2002.

[13]   R. A. Carleton and J. G. Clark, "Measurement of Left Ventricular Diameter In the Dog by Cardiac Catheterization Validation and Physiologic Meaningfulness of an Ultrasonic Technique," *Circulation research,* vol. 22, pp. 545-558, 1968.

[14]   D.-G. Paeng, J. Chang, R. Chen, M. S. Humayun, and K. K. Shung, "Feasibility of rotational scan ultrasound imaging by an angled high frequency transducer for the posterior segment of the eye," *Ultrasonics, Ferroelectrics and Frequency Control, IEEE Transactions on,* vol. 56, pp. 676-680, 2009.

[15]   H. K. Chiang, Q. Zhou, M. S. Mandell, M.-Y. Tsou, S.-P. Lin, K. K. Shung, and C.-K. Ting, "Novel Epidural Needle with Embedded High-frequency Ultrasound Transducer—Epidural Access in Porcine Model," *Anesthesiology,* vol. 114, p. 1320, 2011.

[16]   G. Lockwood, L. Ryan, and F. Foster, "A 45 to 55 MHz needle-based ultrasound system for invasive imaging," *Ultrasonic imaging,* vol. 15, pp. 1-13, 1993.

[17]   Q. Zhou, X. Xu, E. J. Gottlieb, L. Sun, J. M. Cannata, H. Ameri, M. S. Humayun, P. Han, and K. K. Shung, "PMN-PT single crystal, high-frequency ultrasonic needle transducers for pulsed-wave Doppler application," *Ultrasonics, Ferroelectrics and Frequency Control, IEEE Transactions on,* vol. 54, pp. 668-675, 2007.

[18]   Q. Zhou, D. Wu, J. Jin, C. H. Hu, X. Xu, J. Williams, J. M. Cannata, L. Lim, and K. K. Shung, "Design and fabrication of PZN-7% PT single crystal high frequency angled needle ultrasound transducers," *Ultrasonics, Ferroelectrics, and Frequency Control, IEEE Transactions on,* vol. 55, pp. 1394-1399, 2008.

[19]   H.-S. Hsu, F. Zheng, Y. Li, C. Lee, Q. Zhou, and K. K. Shung, "Focused high frequency needle transducer for ultrasonic imaging and trapping," *Applied physics letters,* vol. 101, p. 024105, 2012.

[20]   R. A. Webster, "Passive materials for high frequency piezocomposite ultrasonic transducers," University of Birmingham, 2010.

[21]   W. A. Smith, "The role of piezocomposites in ultrasonic transducers," in *Ultrasonics Symposium, 1989. Proceedings., IEEE 1989,* 1989, pp. 755-766.

[22]   T. Ritter, X. Geng, K. K. Shung, P. D. Lopath, S.-E. Park, and T. R. Shrout, "Single crystal PZN/PT-polymer composites for ultrasound transducer applications," *Ultrasonics, Ferroelectrics, and*

Frequency Control, IEEE Transactions on, vol. 47, pp. 792-800, 2000.

[23]   W. Thiel, "Die Konservierung ganzer leichen in natürlichen farben," *Annals of Anatomy-Anatomischer Anzeiger,* vol. 174, pp. 185-195, 1992.

[24]   S. Cochran, A. Abrar, K. J. Kirk, Z. Dou, T. W. Button, S. Bo, and C. Meggs, "Net-shape ceramic processing as a route to ultrafine scale 1-3 connectivity piezoelectric ceramic-polymer composite transducers," in *Ultrasonics Symposium, 2004 IEEE*, 2004, pp. 1682-1685 Vol.3.

[25]   A. Abrar, D. Zhang, B. Su, T. W. Button, K. J. Kirk, and S. Cochran, "1–3 connectivity piezoelectric ceramic–polymer composite transducers made with viscous polymer processing for high frequency ultrasound," *Ultrasonics,* vol. 42, pp. 479-484, 2004.

[26]   J. Wu, "Determination of velocity and attenuation of shear waves using ultrasonic spectroscopy," *The Journal of the Acoustical Society of America,* vol. 99, pp. 2871-2875, 1996.

[27]   J. M. Cannata, J. Z. Zhao, S. Ayyappan, T. A. Ritter, W. Chen, and K. K. Shung, "Fabrication of high frequency (25-75 MHz) single element ultrasonic transducers," in *Ultrasonics Symposium, 1999. Proceedings. 1999 IEEE*, 1999, pp. 1099-1103.

[28]   G. R. Lockwood, D. H. Turnbull, and F. S. Foster, "Fabrication of high frequency spherically shaped ceramic transducers," *Ultrasonics, Ferroelectrics, and Frequency Control, IEEE Transactions on,* vol. 41, pp. 231-235, 1994.

[29]   Q. Zhou, X. Xu, E. J. Gottlieb, L. Sun, J. M. Cannata, H. Ameri, M. S. Humayun, P. Han, and K. K. Shung, "PMN-PT single crystal, high-frequency ultrasonic needle transducers for pulsed-wave Doppler application," *Ultrasonics, Ferroelectrics, and Frequency Control, IEEE Transactions on,* vol. 54, pp. 668-675, 2007.

[30]   Y. Chen, K.-H. Lam, D. Zhou, Q. Yue, Y. Yu, J. Wu, W. Qiu, L. Sun, C. Zhang, and H. Luo, "High performance relaxor-based ferroelectric single crystals for ultrasonic transducer applications," *Sensors,* vol. 14, pp. 13730-13758, 2014.

[31]   K. Li, "Piezoelectric ceramic fibre/polymer 1-3 composites for transducer applications," The Hong Kong Polytechnic University, 2002.

[32]   J.-Z. Zhao, R. J. Meyer Jr, T. A. Ritter, and K. K. Shung, "Performance of high-frequency PZT fiber composite and PbTiO3 transducers," in *Medical Imaging 2000*, 2000, pp. 100-108.

[33]   R. Eisma, C. Lamb, and R. Soames, "From formalin to Thiel embalming: What changes? One anatomy department's experiences," *Clinical Anatomy,* vol. 26, pp. 564-571, 2013.

[34]   "3D Warehouse - The Brain by Jeroen Hunt. 2009. 3D Warehouse SketchUp." Available at: https://3dwarehouse.sketchup.com/model.html?id=b869d976f c60e9ace4b68d3b17c43658. [Accessed 14 September 15].

[35]   S. Eljamel, A. Volovick, T. Saliev, R. Eisma, and A. Melzer, "Evaluation of Thiel cadaveric model for MRI-guided stereotactic procedures in neurosurgery," *Surgical neurology international,* vol. 5, p. S404, 2014.

[36]   M. J. Gueorguieva, D. T. Yeo, R. Eisma, and A. Melzer, "MRI of thiel‑embalmed human cadavers," *Journal of Magnetic Resonance Imaging,* vol. 39, pp. 576-583, 2014.

[37]   W. Thiel, "Ergänzung für die Konservierung ganzer Leichen nach W. Thiel," *Annals of Anatomy - Anatomischer Anzeiger,* vol. 184, pp. 267-269, 2002.